Patrick Hubert Wagner	Wagner	mail@patrick-wagner.net
First	*Last*	*E-mail*

ECS Paper Title: Towards the Next-Generation of Solid Oxide Fuel Cell Systems

Authors: Vaibhav Singh, Patrick H. Wagner, Zacharie Wuillemin, Stefan Diethelm, Jürg Schiffmann, and Jan Van herle

ECS Conference ECS Conference on Electrochemical Energy Conversion & Storage with SOFC-XIV, Glasgow, UK, July 26-31, 2015

Transactions: ECS Transactions, Volume 68, Number 1, pages 2373-2386

Date of Publication: 2015

DOI: http://dx.doi.org/10.1149/06801.2373ecst

Towards the Next-Generation of Solid Oxide Fuel Cell Systems

V. Singh[a], P. H. Wagner[a], Z. Wuillemin[b], S. Diethelm[ab], J. Schiffmann[a] and J. Van herle[a]

[a] School of Engineering, École Polytechnique Fédérale de Lausanne, Lausanne 1015, Switzerland
[b] HTceramix, Yverdon-les-Bains 1400, Switzerland

To improve the industry benchmark of solid oxide fuel cell systems (SOFC), we consider anode off-gas recirculation using a blower as an add-on to our next-generation SOFC system. Evolutionary algorithms compare the different design alternatives, i.e. co-flow or counter-flow stack operation with hot or cold recirculation. The system performance is evaluated through multi-objective optimization criteria, i.e. maximization of electrical efficiency and cogeneration efficiency. The results obtained suggest that improvements to the best SOFC systems, in terms of net electrical efficiency, are achievable.

Introduction

From the early days of high-temperature (>900 °C) solid oxide fuel cells (SOFCs)[1], the current state-of-the-art SOFCs operate at intermediate temperature regions (i.e. 600-800 °C), and use a nickel-yttria-stabilized zirconia (Ni-YSZ) composite planar anode, a lanthanum strontium cobaltite ferrite (LSCF)/cerium gadolinium oxide (CGO) composite cathode, and a YSZ electrolyte as bulk material. The cell is mostly supported on the anode.[2] Progress has been made in low temperature SOFCs (i.e. 500 °C) using metal supported cells, which are still in an early development stage.[3]

Use of solid oxide fuel cells for power generation is attractive, due to the highest achievable electrical efficiencies in the low power generation range.[4] Nonetheless, there still exists a potential to improve the industry benchmark of SOFC systems, which use natural gas or biogas as fuel and consider steam methane reforming, with external steam supply, for syngas production and usage in the stack. Payne et al.[5] report 60% AC net electrical efficiency for the commercial BlueGen by the company Ceramic Fuel Cells Limited (CFCL). To the authors' knowledge, this is the best SOFC system performance reported.

Anode off-gas recirculation (AOR) using a blower is the add-on to our next-generation SOFC system.[6] Since the recirculating feed contains steam produced in the stack, no external steam supply is needed for reforming. This eliminates the use of expensive water de-ionization sets. Further, it allows for high overall fuel utilization at low diffusion losses. This results in higher cell voltage, and improves the SOFC efficiency.[7] The downside however will be the complexity added with the operation and control of the blower, which could result in unstable stack operation.

Several SOFC systems with AOR have already been demonstrated. Powell et al.[8] operated a SOFC with AOR from 1.65 to 2.15 kW_e with 57% to 53% DC electrical net efficiency. Powell et al. state that the net efficiency could be further improved to over 60% with the use of properly sized blowers. In the framework of the RealDemo–project, the Technical Research Centre of Finland (VTT) operated a 10 kW_e cross-flow SOFC with AOR at an AC net electrical efficiency of 54%.[9,10] All efficiencies in this section are based on the lower heating value (LHV).

Methodology of optimization

The system flowsheet which includes models for balance of plant (BOP) components and an in-house experimentally validated SOFC stack model, is solved using the commercial software Belsim VALI. The design variables identified for this system are 1. oxygen to carbon ratio (O/C) before the external reformer 2. external to total (i.e., external + internal) methane reforming fraction 3. reducing fuel species molar fraction at anode outlet 4. air-fuel equivalent ratio (A/F) in the burner, 5. blower inlet temperature, and 6. blower specific speed.

As shown in Figure 1, there are four steps to optimize the system. This systematic process design methodology is defined in a platform developed for the design and optimization of integrated energy systems called OSMOSE.[11] Firstly, a process flowsheet with models of the individual components is built. The flowsheet is solvable once the values of the previously mentioned design variables are specified. Secondly, using energy integration techniques, internal heat recovery within the system is maximized. Thereafter, performance of the system is evaluated with respect to the desired objectives. Lastly, an iterative optimization procedure is followed, using evolutionary algorithms, where the entire range of design variables is scanned. Successive generations of population are obtained by reproduction and mutation of the existing population. Following the 'survival of the fittest' rule, the iteration is stopped when a non-dominated solution set represented by a Pareto-optimal front is obtained. A similar methodology was used by Facchinetti et al.[12] for the optimization of a SOFC combined with a small-scale gas turbine.

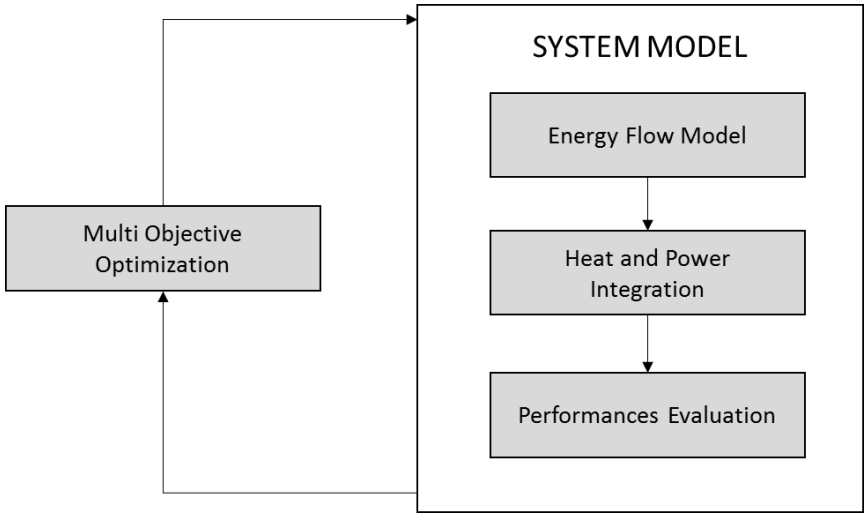

Figure 1. Methodology of the system optimization using OSMOSE

Energy flow model

The system is modeled using the commercial flowsheeting software VALI from Belsim S.A. The system components are the SOFC stack, heat exchangers, reformer, burner, recirculation blower, and fans. The process schematic for a co-flow stack arrangement is shown in Figure 2. Both air and fuel enter the stack at a temperature of 680 ^{o}C and exit at a temperature of 790 ^{o}C. In the counter-flow stack configuration the cathode inlet and outlet are reversed - air and fuel enter from opposite sides. The cathode inlet and outlet temperatures are the same as in the co-flow configuration, but the anode inlet temperature is 790 °C, and the outlet temperature is 680 °C.

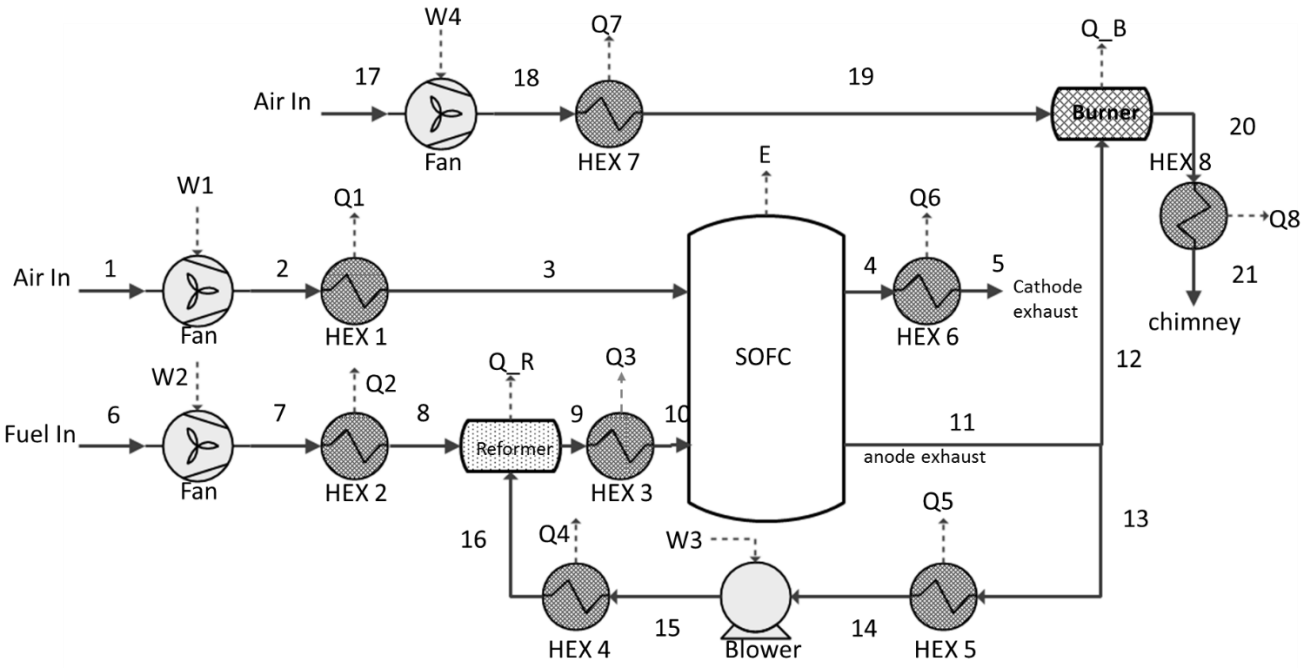

Figure 2. The energy flow model for the SOFC system (co-flow)

Methane (stream 6) and air (stream 1 and stream 17) at a temperature of 20 °C are the feed gases to the system. The fuel is preheated to the reformer temperature (determined by the external to total reforming fraction), where it mixes with the recirculated anode exhaust. Within the isothermal reformer, part of the methane is converted to hydrogen and carbon monoxide. The reforming reaction is completed within the stack (internal reforming). Oxygen from the air feed is consumed in the electrochemical reaction at the cathode. The amount of fuel utilized in the stack is determined by the reducing fuel species fraction set at the anode exhaust. The cathode exhaust is cooled to 60 °C and provides the necessary thermal energy to the system. A fraction of the anode exhaust is sent to the burner, where it undergoes complete combustion with incoming fresh air, which provides the energy balance for the remaining processes in the system. The remaining fraction (determined by O/C ratio in the reformer) is recirculated. Table I describes the design variables and their range of values.

Table I. Decision variables and their range for the multi-objective optimization

Design variables	**Range of values**	**Comments / Constraints**
O/C ratio in external reformer	2-3	Fuel dilution vs carbon deposition
External to total reforming fraction	20-50%	Carbon deposition in anode vs auxiliary power consumption
Reducing species fraction at anode exhaust	10-20%	Oxidation of the Ni-YSZ anode
Air- fuel equivalent ratio in burner	1.1-4.45	System energy balance and maximum temperature in burner
Blower inlet temperature	200 °C 680 °C (counter-flow) 790 °C (co-flow)	Cold recirculation vs Hot recirculation
Blower specific speed	0.2 – 0.8	Low rotational speed and low efficiency vs. High rotational speed and high efficiency

SOFC stack

The SOFC stack model is zero dimensional, to reduce the computational costs involved with genetic algorithms. The model is elaborated in another manuscript.[13] It is an adapted version of the one described in Ref. 14.[14] Further, the model has been validated with the performance maps of HotBox^{TM}, the proprietary stack of HTceramix-SolidPower.[15] Validation with a short stack test is presented in Figure 3. The pressure drop is assumed to be 20 mbar. A constant heat loss of 200 W_{th} based on experimental measurements is included. The efficiency reported in electrical DC stack efficiency.

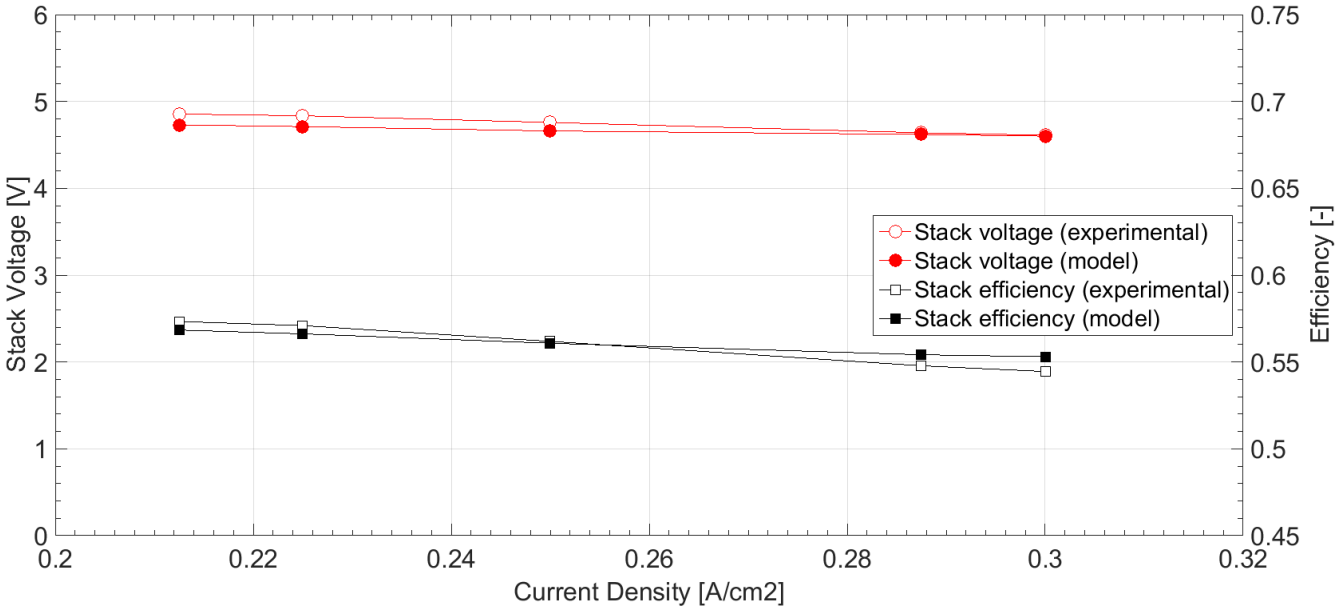

Figure 3. Comparison of experimental and simulated results for a short SOFC stack (6 cells), cell area 80 cm^2, and 75 % fuel utilization

Pre-reformer

The recirculating anode exhaust mixes with the incoming fuel supply just upstream of the reformer. The extent of external methane reforming and water gas shift reaction, considered at equilibrium, is determined by the operating temperature within the reformer. The pressure drop is set to be 30 mbar. A constant heat loss of 100 W_{th} based on experimental measurements is included. The equations for methane reforming and water gas shift reaction are given as:

$$CH_4 + H_2O \rightarrow CO + 3H_2 \quad [1]$$

$$CO + H_2O \rightarrow CO_2 + H_2 \quad [2]$$

Burner

In the burner, the unused fuel from the SOFC stack mixes with fresh air and undergoes complete combustion in adiabatic conditions. The heat released in the process is either used for the energy balance of the system or recovered. The steam in the burner exhaust can be condensed easily due to its higher partial pressure, leading to better cogeneration efficiencies. A pressure drop of 50 mbar is considered in the burner. The equation for the methane, carbon monoxide, and hydrogen combustion are given as:

$$CH_4 + 2O_2 \rightarrow CO_2 + 2H_2O \quad [3]$$

$$CO + 0.5O_2 \rightarrow CO_2 \quad [4]$$

$$H_2 + 0.5O_2 \rightarrow H_2O \quad [5]$$

Heat Exchangers

Counter-flow heat exchangers are modeled. For system compactness and cost reductions, minimum approach temperatures in heat exchangers are restricted to the values mentioned in Table II.

Table II. Constraints on minimum approach temperature

Stream	Minimum approach temperature / 2 (°C)
Gas	25
Cathode	7
Liquid / condensing	15
Reformer	50

Recirculation blower and fans

The efficiencies of the air fan for the burner, as well as the cathode and anode fan are modelled constant. An isentropic efficiency of 60%, a mechanical efficiency of 40%, and an electric motor efficiency of 90% is assumed, resulting in a total efficiency of 22%. Powell et al.[8] report cathode blower efficiencies of 12-15%, but also state that the blowers were not properly sized.

The recirculation blower is modelled in more detail, as the focus is on the AOR. A likewise modelling approach as proposed by Facchinetti et al.[12] is implemented. Analytically derived similarity concepts by Balje[16] are used to calculated the blower isentropic efficiency (η) and the specific diameter (d_s) depending on the specific speed (n_s). These relations are only valid for conservative turbomachinery, implying high Reynolds numbers. Additional losses occurring in small-scale turbomachinery are accounted by Facchinetti et al.[12] with a sensitivity analysis. From the optimal Balje isentropic efficiency a penalty from 0-20% is subtracted.

The approach used here, adds an additional dimension in modelling the blower isentropic efficiency and specific diameter, i.e. the Reynolds number

$$\mathrm{Re} = \frac{\rho \omega \mathrm{Db}}{\mu} = \frac{1}{\pi \phi \mu} \frac{\dot{\mathrm{m}}_{16}}{\mathrm{D}} \quad [6]$$

with the density (ρ) and dynamic viscosity (μ) at the blower inlet, blower rotational speed (ω), blower diameter (D), recirculated mass flow ($\dot{m}_{16}$), blower flow coefficient at the trailing edge (ϕ), and the channel width at the trailing edge (b). A priori the optimized recirculation mass flow and recirculation gas composition are not known. By this, an initial optimization is needed to get a first estimation of these values. The mean values of all points on the Pareto front are used to design a nominal geometry, a radial blower with backward-curved prismatic blades. The resulting nominal Reynolds numbers are up to 60 times lower than that used for the correlation given by Balje, which implies higher viscous losses. The resulting effects are accounted for by using Reynolds correlations given by Wiesner.[17] By this, corrected efficiencies and blower specific diameters can be given as a function of specific speed and a constant nominal Reynolds number. Within the different system designs on the Pareto front, the recirculation mass

flow and therefore the blower diameter vary (higher mass flow implies higher blower diameters and vice versa), wherefore Reynolds numbers differ up to $\pm 40\%$ to the nominal blower geometry. Designing for each iteration of the optimization process a new blower geometry would result in a high computational time, wherefore the values of the nominal geometry are corrected by using a second factor.

$$\eta = 1 - \left(1 - \eta_{\mathrm{nom}}\left(\mathrm{n_s}, \mathrm{Re_{nom}}\right)\right)\left(\frac{\dot{\mathrm{m}}_{16,\mathrm{nom}}}{\mathrm{D_{nom}}}\frac{\mathrm{D}}{\dot{\mathrm{m}}_{16}}\right)^{\gamma} \quad [7]$$

A constant flow coefficient at the trailing edge and constant dynamic viscosity in Equation 6 for each of the different blower designs on the Pareto front are assumed. The exponential factor (γ) normally varies from 0.1 to 0.2 and has to be specified to best fit all the different blower designs on the Pareto front.

The mechanical losses are modelled by assuming gas lubricated journal and thrust bearings. In contrast to conventional ball bearings, the blower life time is increased and the shaft can run at higher rotor speeds and operational temperatures. Loss correlations proposed by Schiffmann[18] are used

$$\mathrm{P_{radial}} = \frac{1}{4}\pi \mathrm{D_{shaft}^3}\omega^2 \frac{\mu \mathrm{L}}{\mathrm{h_{radial}}} \quad [8]$$

$$\mathrm{P_{axial}} = \frac{1}{32}\pi\omega^2\left(\mathrm{D^4} - \mathrm{D_{shaft}^4}\right)\frac{\mu}{\mathrm{h_{axial}}} \quad [9]$$

with the radial bearings length (L), the radial bearing air gap (h_{radial}), the axial bearing air gap (h_{axial}), and the shaft diameter (D_{shaft}). Because no specific optimized bearing design is considered, the losses calculated with Equation 8 and 9 are overestimated. Air at 200° C is assumed as lubricant for the cold, as well as for the hot recirculation. All design parameters can be found in Table III. Windage losses produced in the electric motor air gap are included as proposed by Mack.[19] No specific electric motor design is considered wherefore additional losses, like the iron loss in the stator or the copper loss in the winding[20], are considered with a constant electric motor efficiency of 90%.

Table III. Design parameters for the blower shaft and bearings

Variable	Value	Description
L/D	1	Ratio length to shaft diameter
h_{radial}/D	0.0005	Ratio radial clearance to shaft diameter
h_{axial}/D	0.0015	Ratio axial clearance to shaft diameter
Ndm number	2.5 rpm×mm	Rotational speed multiplied by shaft diameter
h_{mot}	200 μm	Gap in electric motor

Heat and Power integration

Excess heat produced in the system is recovered using water and used for domestic heating. This cold utility undergoes heating from 20 ºC to 60 ºC. No hot utility is needed. Figure 4 shows all the hot and cold system streams of the composite curve.

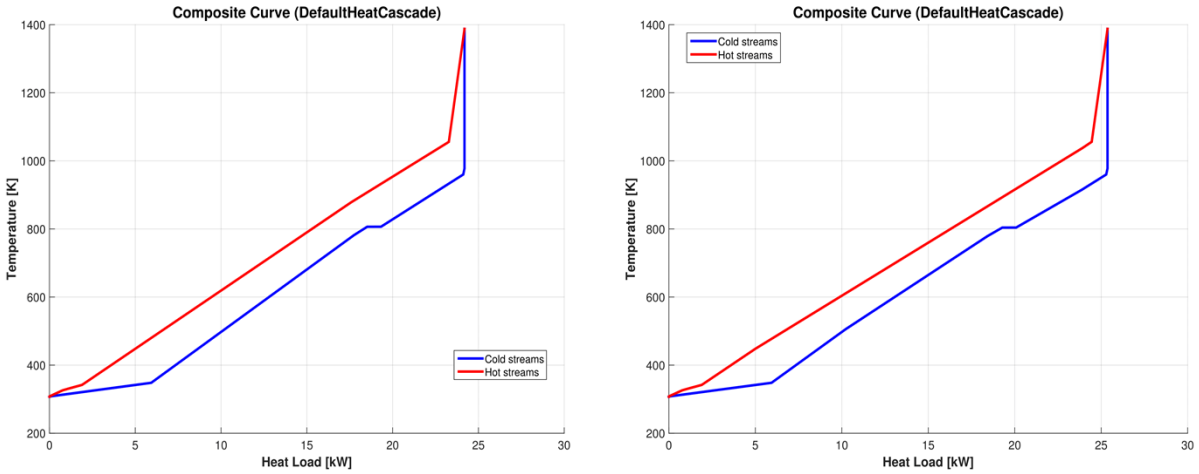

Figure 4. The SOFC system composite curve for hot AOR (left) and cold AOR (right) at the point A, respectively B on the Pareto front shown in Figure 5.

No pinch point is activated in the system process. By this, the potential of exergy recovery is greater than considered in this configuration, but the system is less complex. The area between the composite curves indicates the exergy loss. Figure 4 shows two composite curves for one point of the Pareto Front in Figure 5, point A for the hot AOR and point B for the cold AOR.

Performance objectives and Multi-objective optimization

Within the OSMOSE platform, a queueing multi-objective optimizer (QMOO) based on an evolutionary algorithm is implemented.[21,22] This heuristic algorithm is used for the system optimization. Starting with an initial population of randomly assigned genes (i.e. the values of the six decision variables), the flowsheet is solved for each individual. This initial population size is chosen to be 200. The members are evaluated based on the system DC net electrical efficiency

$$\eta_e = \frac{(E - W1 - W2 - W3 - W4)}{\dot{m}_6 \times LHV} \quad [10]$$

and the cogeneration efficiency

$$\eta_c = \frac{(E - W1 - W2 - W3 - W4) + \sum Q}{\dot{m}_6 \times LHV} \quad [11]$$

with the SOFC electrical output (E), the auxiliary equipment electrical consumption (W1, W2, W3, and W4), and the sum of heat flows (Q). These streams are shown in Figure 2. After 5000 iterations the Pareto front is considered to be converged.

Results and analysis

Figure 5 shows the results obtained after non-dominated solution sets are obtained with evolutionary algorithms for the case of co-flow and counter-flow stack operation (10 kW_e electrical output) with cold recirculation (i.e. 200 °C) or hot recirculation (i.e. anode exhaust temperature). Co-flow stack operation with cold recirculation gives the best performance, as the recirculation blower consumes less work with cooler fluids. Net DC electrical efficiencies in excess of 64% are achievable. Contrary to the co-flow stack model, the results of the counter-flow model remain unvalidated at this stage with experiments, and will be elaborated in later manuscripts. Henceforth, only the detailed results of co-flow stack configuration will be presented.

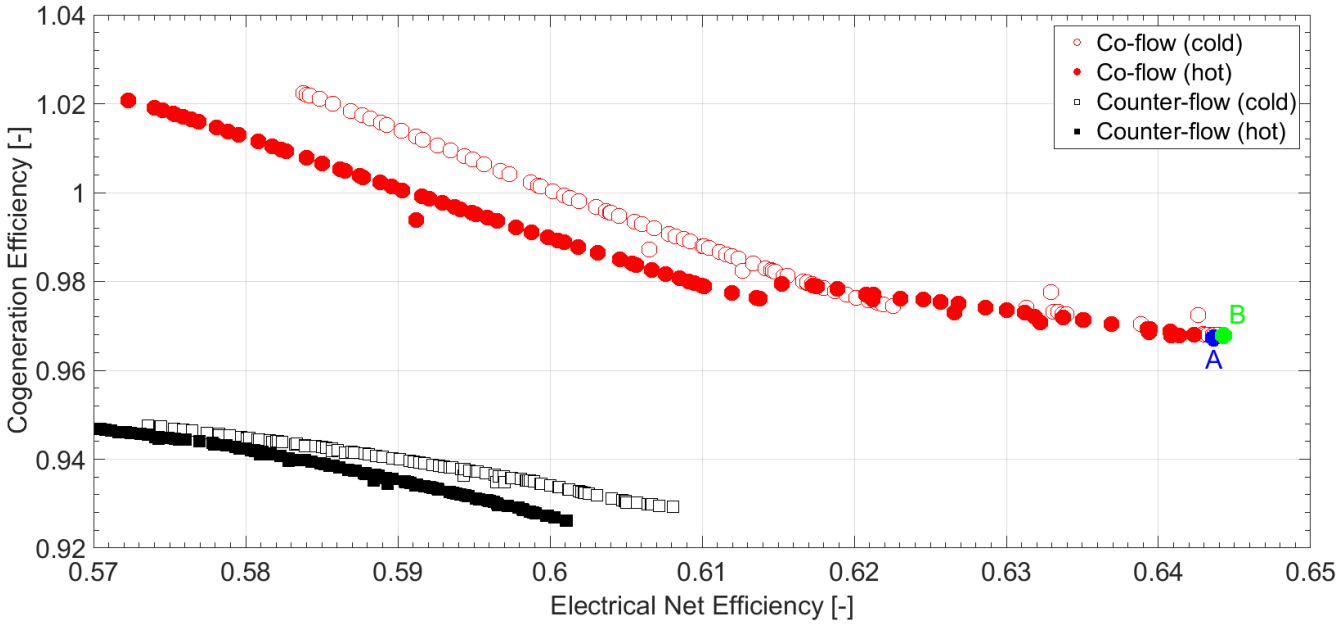

Figure 5. Pareto front of the optimized SOFC system

With increasing electrical net efficiency, fuel utilization increases, irreversible losses increase and consequently the cell voltage goes down. To account for the same stack power output of 10 kW_e, the number of cells in the stack increases. This is shown in Figure 6. There is a discontinuity around the 62 % electrical efficiency region, where the system switches from a lower local fuel utilization and higher recirculation operation to a higher local fuel utilization and lower recirculation operation, as shown in Figure 7. This accounts for the sudden voltage jump.

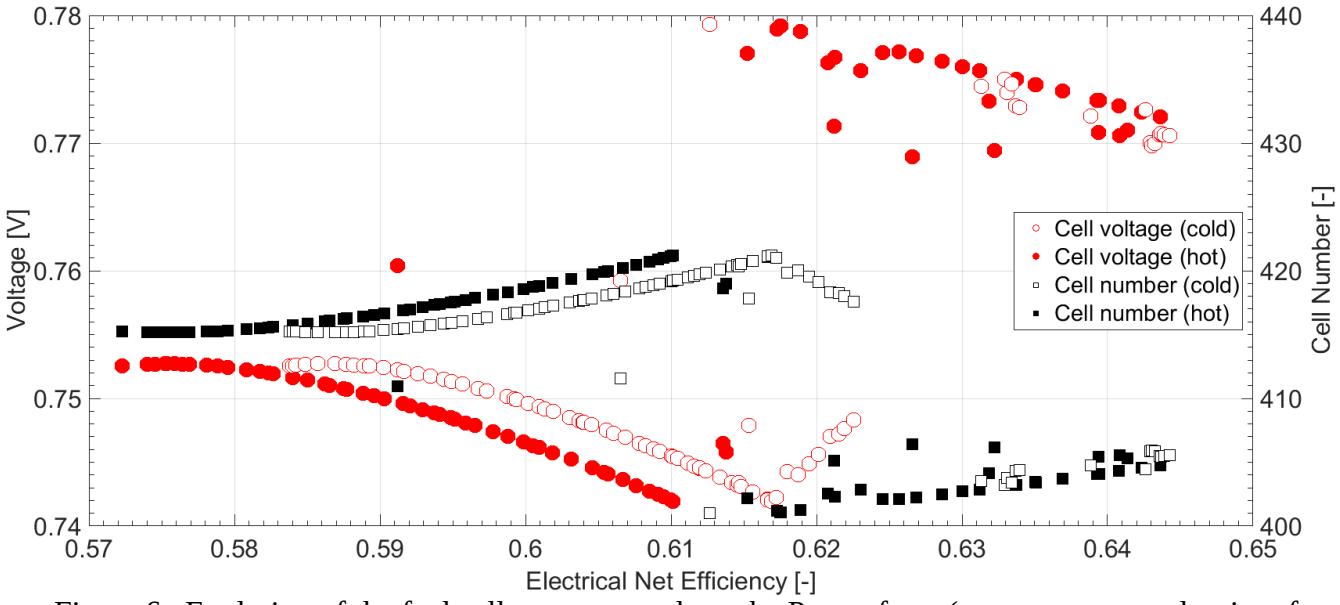

Figure 6. Evolution of the fuel cell parameters along the Pareto front (constant current density of 0.4 A/cm²)

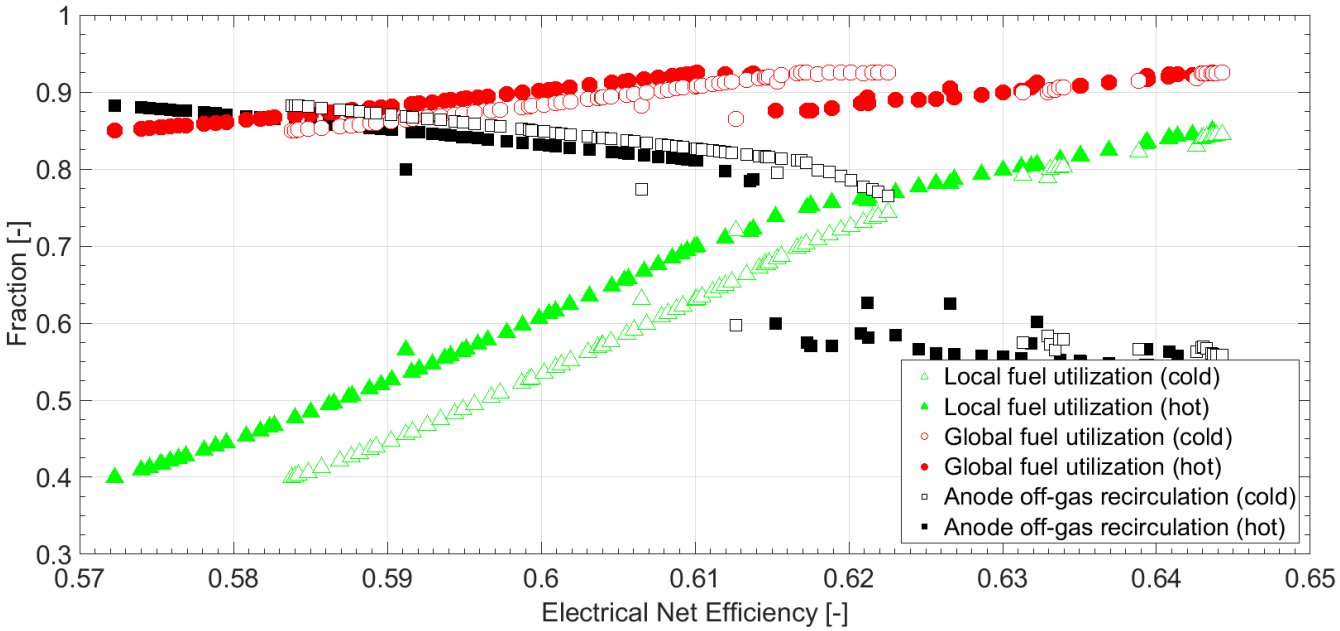

Figure 7. Evolution of anode off-gas recirculation, local and global fuel utilization along the Pareto front

Increase in system electrical net efficiency leads to greater stack heat generation. To maintain the stack temperature gradient, the cathodic air flow increases. Less fuel is available for the system energy balance and extra heat, and therefore the adiabatic flame temperature in the burner decreases (see Figure 8). The reformer temperature tends towards the required lower external reforming limit of 20%, based on an isothermal equilibrium model. This is shown in Figure 9.

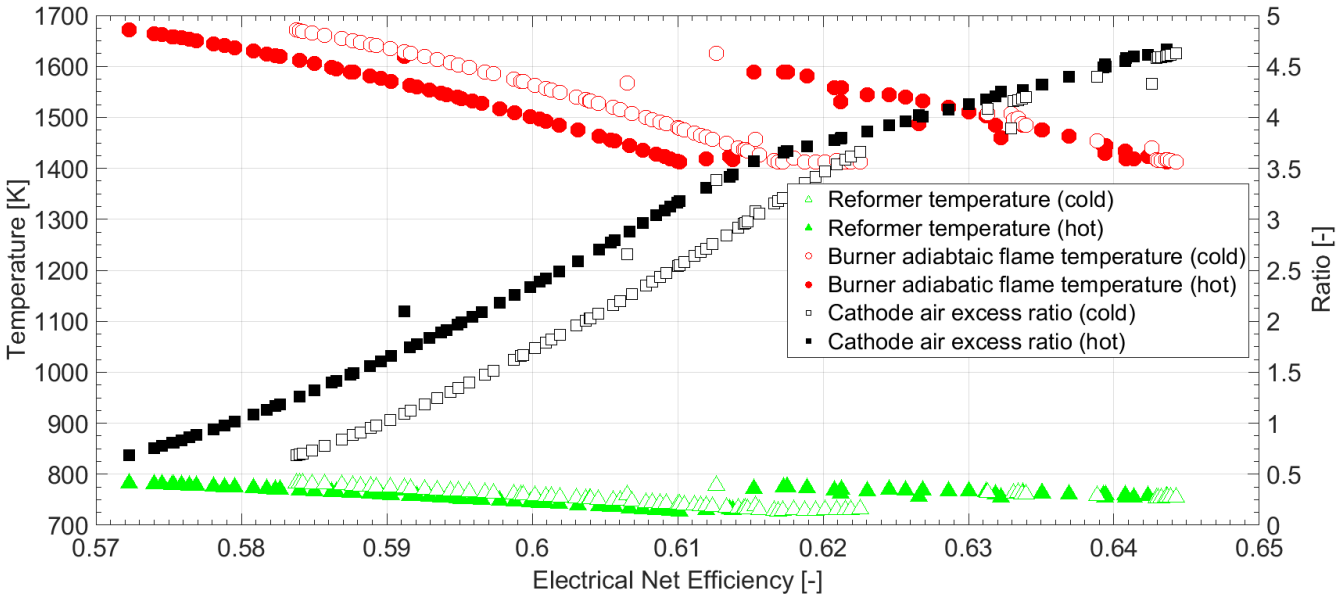

Figure 8. Evolution of system temperatures and cathode air excess ratio along the Pareto front

The fraction of reducing species (i.e. H_2 and CO) at the anode outlet reach the lower limit of 10% for a better fuel utilization and electrical efficiency. The external to total reforming fraction of 20% is also the lower limit, as a higher endothermic internal reforming neutralizes the stack heat and reduces cathodic blower losses. An O/C ratio of 3 in reformer corresponds to higher recirculation and lower local fuel utilization operation. As the operation mode switches, the O/C ratio in the reformer switches to the lower value of 2. This is shown in figure Figure 9.

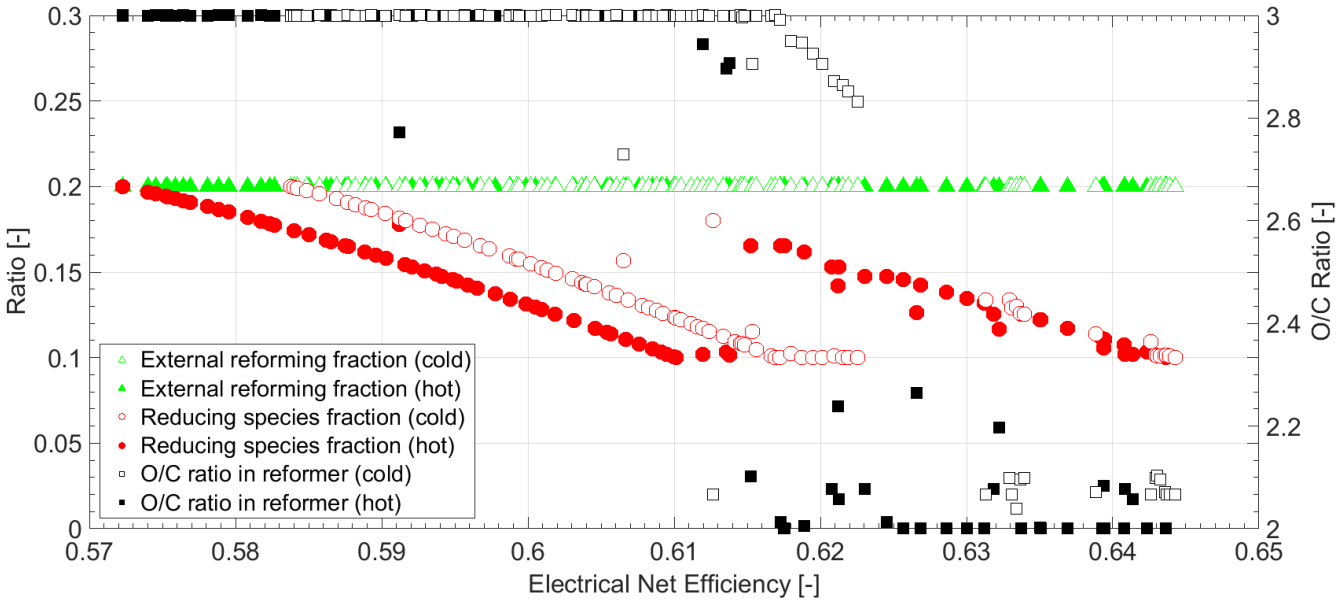

Figure 9. Evolution of three design variables along the Pareto front

For all configurations the specific speed converges towards 0.8, wherefore high-speed turbomachinery is favored. According to the Balje correlations, the isentropic efficiency is 87% at a specific speed of 0.8.

Figure 10 shows the evolution of the blower isentropic, mechanical and total efficiencies which also includes the electric motor efficiency of 90%. At the nominal blower design point, at 61% electrical net

efficiency, the corrected isentropic efficiency is 16% (cold recirculation) and 22% (hot recirculation) lower than the optimal Balje efficiency. The difference of 6% between hot and cold recirculation is mainly due to higher dynamic viscosities and lower densities at high temperatures, resulting according to Equation 6 in lower Reynolds numbers and therefore higher viscous losses. To the left of the nominal blower design at 61% electrical net efficiency, the increase of the AOR is higher than that of the blower diameter (Figure 7 and Figure 11), wherefore the isentropic efficiency slightly increases according to Equation 7, and vice versa to the right. The isentropic efficiency of 60% to 68% for the hot recirculation matches to the efficiencies reported by Johnson.[23]

Although the total efficiency of the hot recirculation blower is higher than that of the cold recirculation blower, the electrical power input for the hot AOR is higher (505-120 W_e) compared to the cold AOR (318-92 W_e). The main mechanical losses occur in the radial bearings (hot AOR: 118-46 W, cold AOR: 145-60 W). The high values of the electrical power and losses previously mentioned, refer to the left side of the Figure 10, e.g. low electrical net efficiencies, and vice versa.

As shown in Figure 11, for low AOR, the blower diameter is higher and the rotational speeds lower than for high AOR. Rotational speeds are up to 150 krpm (hot AOR) and 120 krpm (cold AOR) to ensure the pressure increase of 50 mbar. Blower diameters of 28 (hot AOR) to 24 mm (cold AOR) are very feasible in terms of manufacturing as already has been shown by Schiffmann and Favrat.[24]

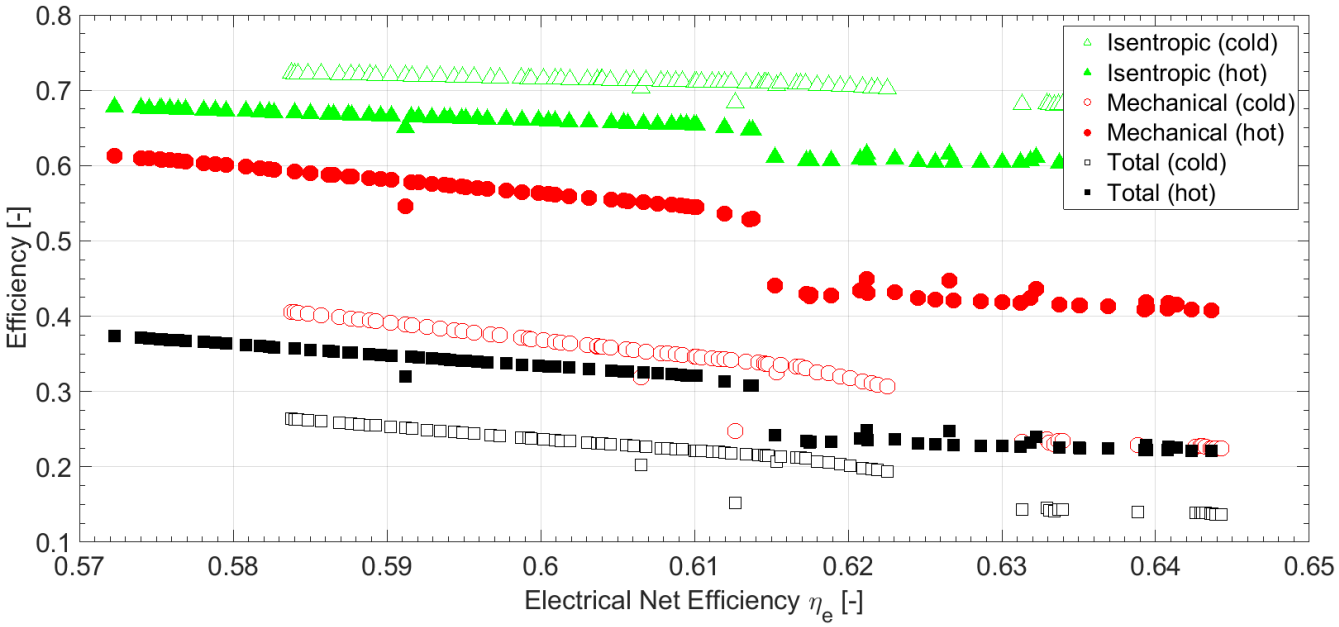

Figure 10. Evolution of blower efficiencies along the Pareto front

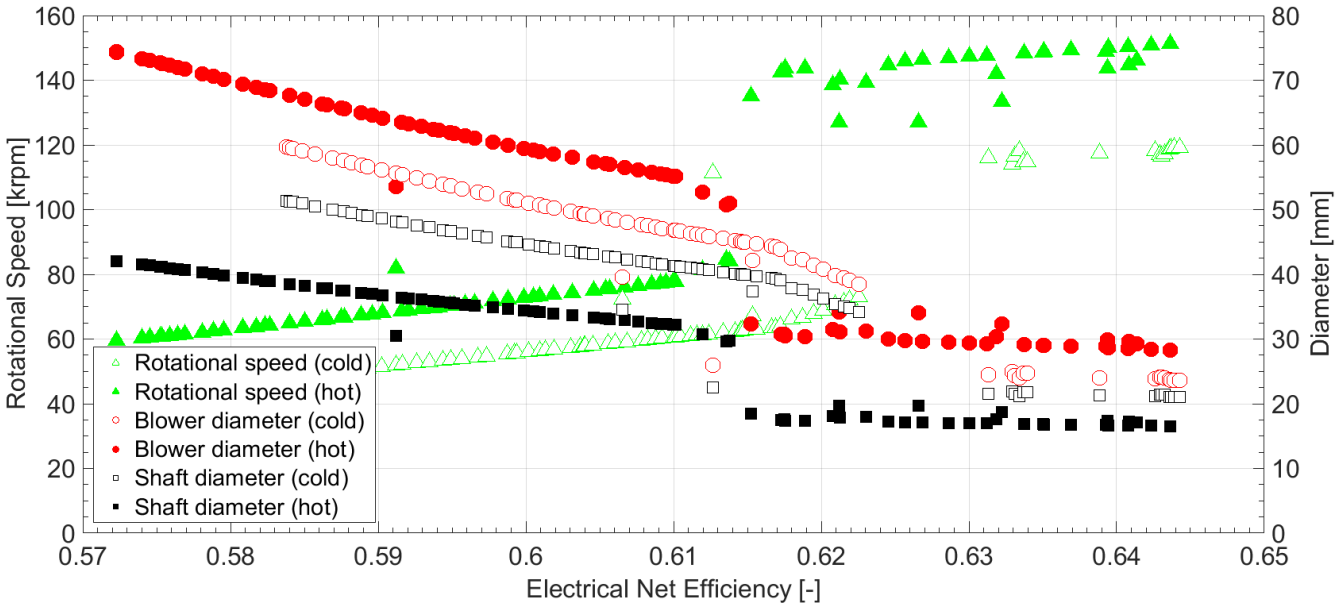

Figure 11. Evolution of blower rotational speeds, blower and shaft diameter along the Pareto front

The operation characteristics of the system, at the chosen point of maximum electrical efficiency, i.e. point A for hot AOR and point B for cold AOR as shown in Figure 5, are summarized in Table IV.

Table IV. Operation characteristics of system at best electrical efficiency point

	Hot AOR (point A)	**Cold AOR (Point B)**
SOFC stack electrical output (DC)	10 kW_e	10 kW_e
Net electrical efficiency (LHV DC)	63%	64.4%
Cogeneration efficiency (LHV)	97.4%	96.8%
No. of cells in stack	403	406
Cell voltage	0.776 V	0.771 V
Current density	0.4 A/cm²	0.4 A/cm²
Cell area	80 cm²	80 cm²
Blower specific speed	0.8	0.8
Blower speed	147.3 krpm	124.7 krpm
Blower diameter	29.4 mm	23.6 mm
O/C ratio at reformer inlet	2	2.07
Reducing species fraction at anode exhaust	0.135	0.10
External to total reforming fraction	0.2	0.2
Blower inlet temperature	790 °C	200 °C
Mass flow rate methane (at 20 °C)	0.297 g/s	0.292 g/s
Air excess	4.13	4.63
Single pass fuel utilization	79.8%	84.5%
Global fuel utilization	89.9%	92.5%
Anode off-gas recirculation fraction	55.6%	55.8%
Pressure drop in SOFC stack	20 mbar	20 mbar
Power consumption in recirculator	120 W_e	92 W_e
Power consumption cathode fan	456 W_e	486 W_e
Heat exchanged Q_R	-0.813 kW_{th}	-0.797 W_{th}
Heat exchanged Q1	-16.7 kW_{th}	-17.8 kW_{th}
Heat exchanged Q3	-0.796 kW_{th}	-0.839 kW_{th}
Heat exchanged Q_B + Q8	4.911 kW_{th}	4.365 kW_{th}
Heat exchanged Q4	0.519 kW_{th}	-1.14 kW_{th}
Heat exchanged Q5	0 kW_{th}	1.68 kW_{th}
Heat exchanged Q6	18.1 kW_{th}	19.3 kW_{th}

Conclusion

Thus, evolutionary algorithms can aid in the optimization of SOFC systems. Co-flow stack operation with cold recirculation seems to be the best operation strategy. Hot recirculation at high net electrical efficiency is also promising. This could possibly save some investment cost by avoiding the additional heat exchangers needed for cooling and heating of AOR. The zero dimensional counter-flow model is yet to be validated with experiments. It is shown that electrical efficiencies well in excess of 60% can be achieved.

Minimisation of system costs will be included as a 3rd objective for multi-objective optimization of this system in future, for designing a more market oriented system. Inclusion of realistic pressure losses in system components will better estimate auxiliary power losses. A more detailed model for the stack will replace the current zero-dimensional stack model created in Belsim VALI. This will however compete with the computational complexity involved in evolutionary algorithms. Lastly, a transient fuel cell model, incorporating degradation mechanisms, could aid in dynamic operation strategy to maximise durability and long term performance.

Acknowledgement

The authors would like to acknowledge the support of Siu Fai and Mardit Matian from HTceramix, as well as Isha Shukla and Arata Nakajo from EPFL in aiding the work. This work would not have been possible without the software license from Belsim S.A., and the research grant from Canton de Vaud under the ‘100 million de francs pour les énergies renouvelables et l'efficacité ènergétique’.

References

1. Y. Zhao et al., *Int. J. Hydrog. Energy*, **38**, 16498–16517 (2013).

2. S. C. Singhal, *Wiley Interdiscip. Rev. Energy Environ.*, **3**, 179–194 (2014).

3. R. Leah et al., in, vol. 57, p. 461–470 (2013).

4. E. Facchinetti, PhD thesis, EPFL, Lausanne (2012).

5. R. J. Payne, J. Love, and M. Kah, *ECS Trans.*, **35**, 81–85 (2011).

6. N. Autissier, PhD thesis, EPFL, Lausanne (2008).

7. R. Peters et al., *Int. J. Hydrog. Energy*, **38**, 6809–6820 (2013).

8. M. Powell, K. Meinhardt, V. Sprenkle, L. Chick, and G. McVay, *J. Power Sources*, **205**, 377–384 (2012).

9. M. Halinen et al., *ECS Trans.*, **35**, 113–120 (2011).

10. M. Halinen, A. Pohjoranta, L. Kujanpää, V. Väisänen, and P. Salminen, *Summary of the RealDemo – project 2012-2014*, VTT Technical Research Centre of Finland, (2014).

11. F. Palazzi, N. Autissier, F. M. A. Marechal, and D. Favrat, *Appl. Therm. Eng.*, **27**, 2703–2712 (2007).

12. E. Facchinetti, D. Favrat, and F. Marechal, *Fuel Cells*, **14**, 595–606 (2014).

13. V. Singh, I. Shukla, Z. Wuillemin, St. Diethelm, and J. van Herle, in, Pau, France (2015).

14. Van herle Jan, F. Maréchal, S. Leuenberger, and D. Favrat, *J. Power Sources*, **118**, 375–383 (2003).

15. S. Modena et al., *ECS Trans.*, **57**, 359–366 (2013).

16. O. E. Balje, *Turbomachines : a guide to design, selection and theory*, New York a.o. : Wiley, (1981).

17. F. J. Wiesner, *ASME Trans. J. Eng. Power*, **101**, 384–392 (1979).

18. J. Schiffmann, PhD thesis, EPFL, Lausanne (2008).

19. M. Mack, PhD thesis, T. H., F. f. Maschinenw., Stuttgart (1967).

20. C. Zwyssig, S. D. Round, and J. W. Kolar, in *Conference Record of the 2006 IEEE Industry Applications Conference, 2006. 41st IAS Annual Meeting,*, vol. 3, p. 1507–1513 (2006).

21. G. Leyland, PhD thesis, EPFL, Lausanne (2002).

22. A. Molyneaux, PhD thesis, EPFL, Lausanne (2002).

23. M. C. Johnson, *R-MCJ10042201-1A_PADT_PhaseII-report-final*, Phoenix Analysis & Design Technologies, United States, (2010) http://www.osti.gov/scitech/servlets/purl/1122082.

24. J. Schiffmann and D. Favrat, *Energy*, **35**, 436–450 (2010).